applied sciences

MDPI

Article

Analysis of 3D Printed Dielectric Resonator Antenna Arrays for Millimeter-Wave 5G Applications

Siyu Li [1], Benito Sanz Izquierdo [1,*], Steven Gao [2] and Zhijiao Chen [3]

[1] School of Engineering, University of Kent, Canterbury CT2 7NZ, UK
[2] Department of Electronic Engineering, Chinese University of Hong Kong, Hong Kong 518057, China; scgao@ee.cuhk.edu.hk
[3] Department of Electronic Engineering, Beijing University of Posts and Telecommunications, Beijing 100876, China; z.chen@bupt.edu.cn
* Correspondence: b.sanz@kent.ac.uk

Abstract: This paper explores the potential use of fused deposition modeling (FDM) technology for manufacturing microwave and millimeter-wave dielectric resonator antennas (DRAs) for 5G and beyond communication systems. DRAs operating at microwave and millimeter-wave (mmWave) frequency bands were simulated, fabricated, and analyzed in terms of manufacturing quality and radio frequency (RF) performance. Samples were manufactured using a 3D printer and PREPERM® ABS1000 filament, which offers a stable dielectric constant ($\varepsilon_r = 10 \pm 0.35$) and low losses ($\tan\delta = 0.003$) over wide frequency and temperature ranges. Surface profile tests and microscope measurements revealed discrepancies in the dimensions in the xy-plane and along the z-axis, consistent with the observed shift in resonant frequency. Despite these variations, reasonably good agreement between RF-simulated and measured results was achieved, and the DRA array successfully covered the intended mmWave band. However, challenges in achieving high precision may restrict applications at higher mmWave bands. Nevertheless, compared with conventional methods, FDM techniques offer a highly accessible and flexible solution with a wide range of materials for home and micro-manufacturing of mmWave DRAs for modern 5G systems.

Keywords: fused deposition modeling; additive manufacturing; 3D printing; dielectric resonator antenna; surface profile

Citation: Li, S.; Sanz Izquierdo, B.; Gao, S.; Chen, Z. Analysis of 3D Printed Dielectric Resonator Antenna Arrays for Millimeter-Wave 5G Applications. *Appl. Sci.* **2024**, *14*, 9886. https://doi.org/10.3390/app14219886

Academic Editor: Christos Bouras

Received: 22 September 2024
Revised: 21 October 2024
Accepted: 23 October 2024
Published: 29 October 2024

1. Introduction

The advent of 5G technology has created a pressing need for advanced antenna systems capable of supporting higher frequencies and larger bandwidths. Dielectric resonator antennas (DRAs) have emerged as a promising solution due to their low-loss characteristics, high radiation efficiency, and ability to operate at millimeter-wave frequencies [1]. Since their introduction in 1983 [2], DRAs have been extensively researched in the fields of antennas and propagation, leveraging various materials and manufacturing techniques to optimize performance. Traditional methods using ceramic rods could typically offer high permittivity, ranging over 20, but it is less likely to achieve designs with permittivity below 20 [3,4]. This would lead to limited choices in materials as well as design freedom. Other methods apply compound dielectric materials, such as printable dielectric ink [5], flexible magnetic polymer composite substrates with equal permittivity and permeability [6], and mixtures of silicone rubber and barium strontium titanate nanoparticles [7]. However, most compound dielectric materials need to be synthesized through complex processes, which increase the complexity and cost of the overall design.

Additive manufacturing (AM), also known as 3D printing, is an emerging technology that has attracted significant attention from both the academic community and industry over the past few decades [8–16]. It offers advantages such as low cost, high design flexibility, rapid prototyping, reduced material waste, etc., and has been applied exclusively

in manufacturing different components across various fields. Recent advancements in AM technologies have significantly expanded its applications and capabilities. Techniques such as stereolithography (SLA), selective laser sintering (SLS), fused deposition modeling (FDM), and direct metal laser sintering (DMLS) have evolved, offering enhanced precision, material diversity, and functional properties [17–22]. The development of multi-material printing has further pushed the boundaries, allowing the creation of complex structures with varying mechanical properties within a single build [23–26].

AM techniques have recently been applied to RF designs, including antennas, for various purposes across different applications [27–32]. The integration of AM techniques into DRA manufacturing represents a significant advancement, enabling the production of complex geometries and customized designs previously unattainable with conventional methods. AM offers the capability to rapidly prototype and test various DRA designs, significantly reducing the time and cost associated with traditional manufacturing processes. Recent progress in using AM techniques to produce DRAs has been reported [33–35]. Five DRA samples were fabricated using two AM technologies, namely FDM and SLA, for 5G applications [33]. The FDM technique and the spatial variant lattices (SVL) synthesis algorithm were combined to design two inhomogeneous DRAs with linearly varying permittivity profiles along their radial and vertical axes [34]. Super-shaped DRAs were manufactured using inverted micro-SLA. DRA prototypes with basic cross-star shape geometries were manufactured by considering different twist angles along the vertical axis [35]. In general, different AM techniques have been applied to manufacture DRAs in recent years, while more details, such as surface profile, manufacturing resolution, and practical applications, remain to be explored. Although other commonly used AM techniques are rarely applied to DRA manufacturing, they have proven feasible for manufacturing other RF devices and show great potential for DRA fabrication. Examples include flat panel antennas using SLS [36], waveguide antennas using DMLS [37] or binder jetting [38], and rectangular cavity resonators using material jetting [39].

This paper discusses the feasibility of using off-the-shelf FDM technology to manufacture low-cost DRA arrays. By utilizing an easily accessible 3D printer and low-cost, flexible filaments, several DRA samples operating at microwave or mmWave were designed and manufactured. These samples were then analyzed using a portable microscope to examine the surface profile and provide detailed information about the fabrication process. Good agreement between the simulated and measured results, as well as surface profile figures, proves the feasibility of using FDM techniques to develop DRAs. The successful application of FDM in DRA manufacturing could revolutionize the production of antenna arrays, making them more accessible and adaptable to the rapid advancements in wireless communication technologies.

2. 3D Printed DRA at Microwave Frequency

A DRA operating within the microwave frequency band at 13.2 GHz was designed to initially test the FDM feasibility. The DRA design is depicted in Figure 1. The radius (r_d) and height (h_d) of the DRA are 3.075 and 2.625 mm, respectively. The resonant frequency of the $TE_{01\delta}$ mode of a cylindrical DRA can be calculated by [40],

$$f = \frac{2.921c\varepsilon_r^{-0.465}}{2\pi r}\left[0.691 + 0.319x - 0.035x^2\right] \quad (1)$$

where c is the speed of light, $x = r/2h$, ε_r, r, and h are the relative permittivity, radius, and height of the DRA, respectively. The substrate used is the RT Duroid 5880 (ε_r = 2.2) with a thickness of 0.51 mm and a dimension of 20 mm × 20 mm. The DRA has a relative permittivity ε_r = 10. It is slot-fed by a microstrip line with an impedance of 50 ohms to ensure better matching with the SMA connector. The slot has a length (l_s) of 3.2 mm and a width (w_s) of 0.5 mm, and the feeding line measures 13 mm in length (l_{ms}) and 1.6 mm in width (w_{ms}).

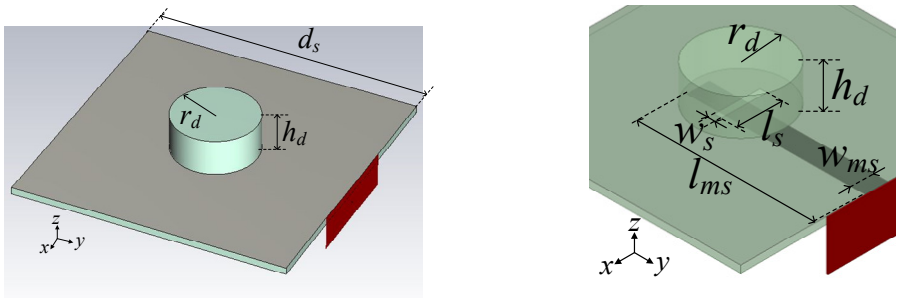

(**a**) (**b**)

Figure 1. Configuration of the FDM printed microwave DRA: (**a**) DRA on top of a metallic ground plane, (**b**) substrate and DRA made transparent to show the microstrip transmission line on the back of the substrate and the slot on the top ground plane.

A set of such DRAs were manufactured using the widely available FDM Raise E2 3D printer (Shanghai, China) and a low-loss dielectric thermoplastic filament. A 0.4 mm nozzle was used with an extrusion temperature of 250 °C and a heated bed at 80 °C during the printing process. The filament diameter was 1.75 mm, and the layer thickness was set to 0.2 mm. Four DRAs with 100% infill were printed in parallel orientation to the bed during each batch, with a printing speed of 60 mm/s. The PREPERM® ABS1000 filament, manufactured by Avient Corp. (Liverpool, UK), was used in this work. This filament provides a stable dielectric constant, ε_r, of 10 $\pm$ 0.35 across a wide range of frequencies and temperatures, with a loss tangent, tan δ, of about 0.003. The standard resolution provided by the manufacturer of this machine exceeds 0.2 mm along the z-axis and 0.4 mm along the xy-axis.

Figure 2 displays the photo of the printed DRA element. Surface profiles and photos were taken using a KEYENCE VHX-7000 series portable microscope (KEYENCE (UK) Ltd., Milton Keynes, UK), which offers a large depth of field, high resolution, and up to 6000× magnification. The results are shown in Figures 2–4. Thirteen uniform layers of about 0.2 mm height were required and observed to achieve the total height of 2.6 mm of the microwave DRA. Reasonably smooth surfaces were observed, considering the expected resolution of about 0.2 mm for FDM printing. As seen in Figure 3, the DRA is relatively consistent with the simulation model in overall shape. Protuberances with a maximum height of the profile (R_z) of 112.01 µm and an arithmetic average roughness (R_a) of 28.38 µm can be observed in the 3D side view and 2D cut surface profile shown in Figure 4. R_z and R_a are commonly used to evaluate surface profile, as defined by the ISO 4287 standard [41]. These values reflect the protuberances and uneven surface along the sides of the DRA. Some air gaps could also be observed. These errors and residuals may lead to a lower equivalent relative permittivity of the overall structure and thus a frequency shift to a higher band.

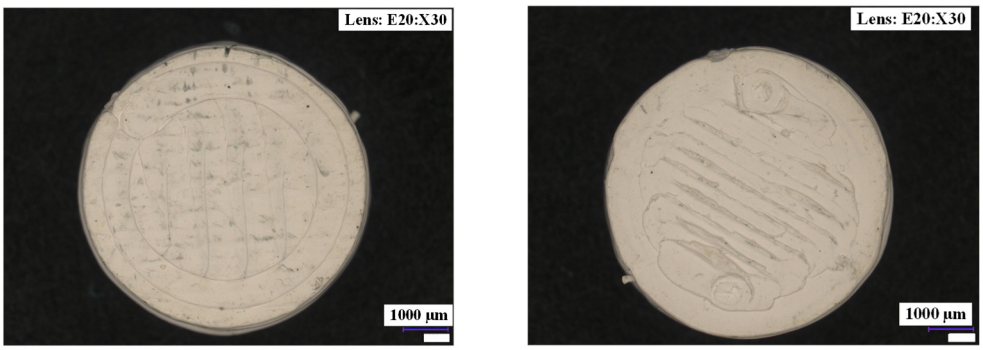

(**a**) (**b**)

Figure 2. Zoom-in view of the top and bottom surfaces of the FDM-printed microwave DRA. (**a**) top view, (**b**) bottom view.

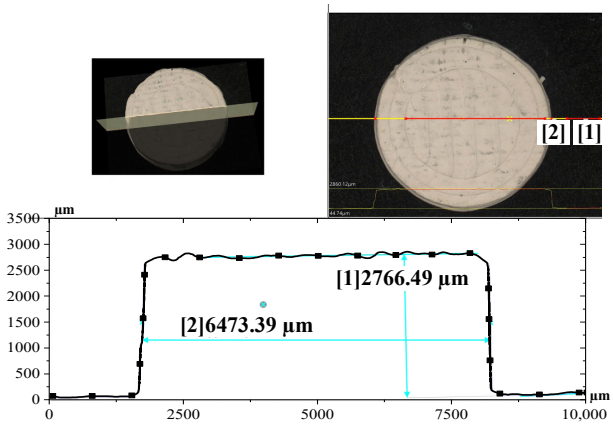

Figure 3. 2D cut surface profile of the FDM-printed DRA.

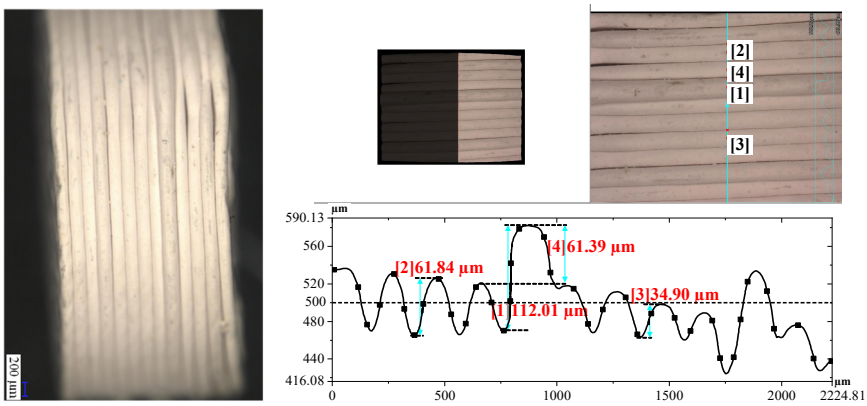

Figure 4. 3D side view and 2D cut surface profile of the FDM-printed DRA.

The design simulation was performed using the EM simulator Ansys HFSS (Ansys, Inc., Canonsburg, PA, USA). All the dimensional parameters of the DRA mentioned above are consistent with those used in the simulation model. The FDM 3D-printed DRA was then fabricated on a PCB with an integrated connector, as shown in Figure 5. The *S*-parameters were measured using a Keysight P9377B network analyzer (Keysight Technologies UK, Wokingham, UK), and the results are shown in Figure 6. A good agreement between the simulated and measured results was observed with just a slight shift from 13.2 GHz to 13.5 GHz (2.3%). To identify the possible reasons, the measured dimensional parameters (Figure 3) were applied to the simulation model. After adjusting the radius and height of the DRA to match the measured values, the resonant frequency shifted downward, which is expected due to the increased dimensions. However, the presence of an air gap may result in a lower equivalent permittivity. By reducing the permittivity of the material in the simulation model by 8%, the simulated *S*-parameters of the DRA align more closely with the measured results. Other potential errors unrelated to 3D printing, such as the placement of the DRA or gaps between the DRA and feeding slot, may also have affected the resonant frequency. The simulated and measured Q factors are 23.57 and 37.50, respectively.

Overall, the performance of the FDM 3D-printed DRA meets the requirements for microwave frequency applications within an acceptable error range. The 13 GHz frequency band is commonly used in satellite communications, radar systems, and point-to-point communication links. However, the focus of this study is to investigate the 3D printing technique; therefore, the specifications are not strictly governed by any standard. Considerations such as increased size after printing and potential reduction of permittivity due to air gaps need to be taken into account at the Ku-band and higher microwave frequency bands.

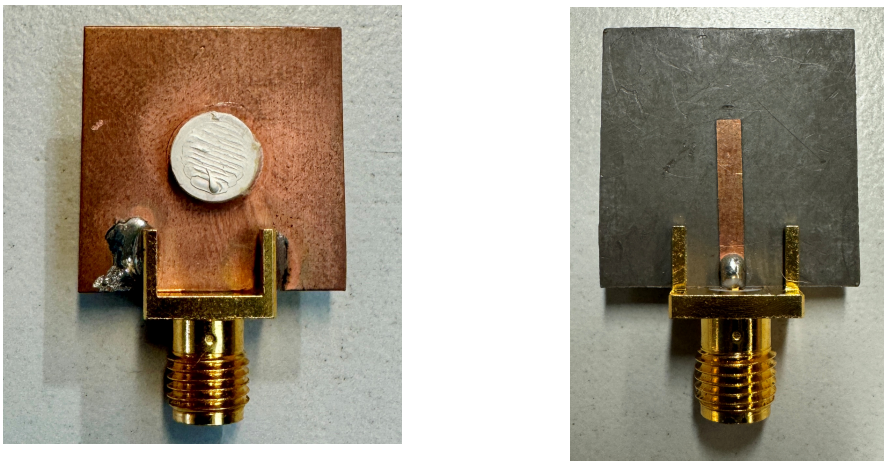

(**a**) (**b**)

Figure 5. Fabricated DRA. (**a**) top view, (**b**) bottom view.

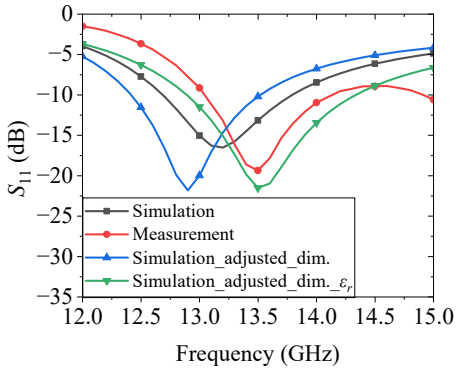

Figure 6. Simulated and measured S_{11} of the microwave DRA design. Adjusted dimensional parameters and permittivity were also taken into account based on the measured values.

3. Millimeter-Wave DRA Array for 5G Systems

In DRA arrays operating at mmWave frequencies, every single DRA element needs to be fabricated with sufficient accuracy for the array to perform well. To assess the quality and reliability of the FDM technology in producing the DRAs at such frequencies, a 2 × 2 DRA array working at the mmWave band for beam scanning applications was designed, simulated, manufactured, and measured. The configuration is shown in Figure 7. The substrate applied in simulation and fabrication is Rogers RO4003 (ε_r = 3.55, tan δ = 0.0027) with a height of 0.2 mm. The DRA elements have a cylindrical shape with a dimension of Ø3.2 mm (r_d) × 1.9 mm (h_d). These dimensional parameters are frequency-dependent and determine the resonant frequency of the DRA. As indicated by Equation (1), higher frequency bands result in smaller DRA dimensions. The parameters provided here have been optimized for both matching and radiation performance. The distance (d) between two adjacent DRA elements is 6 mm. Each DRA element is slot-fed by a microstrip line, allowing for variable excitation during the initial simulation process. The beam scanning performance of the DRA array can be preliminarily verified by varying the excitation amplitude and phase through the four lumped ports connected to the microstrip lines, as shown in Figure 7. The slot measures 1.8 mm in length (l_1) and 0.2 mm in width (w_1), providing an efficient coupling mechanism between the microstrip feed and the DRA element. The width (w_2) of the microstrip line is designed to be 0.45 mm, ensuring a 50-ohm impedance for optimal matching performance with the rest of the system, including the SMA connectors. A matching stub with a length (l_2) of 1.5 mm was introduced to improve impedance matching and enhance coupling. This configuration minimizes reflection and maximizes power transfer to the DRA, thereby enhancing overall efficiency.

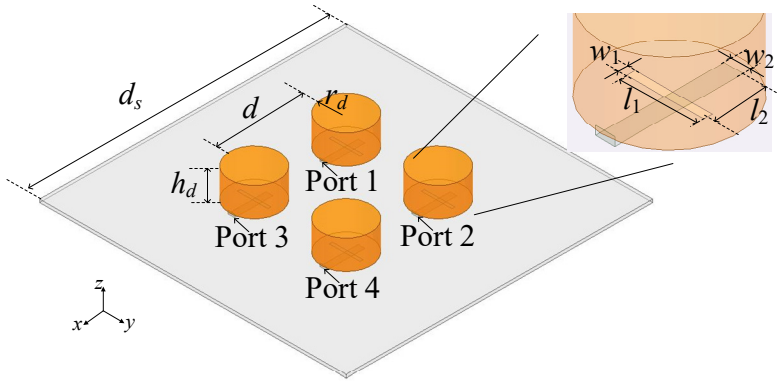

Figure 7. Configuration of the mmWave DRA array.

Total efficiency, rather than single-ended S-parameters, was considered to evaluate the matching performance of the DRA array due to the insufficient representation of individual S-parameters in multi-port antenna arrays. Further details on the S-parameters are provided in the full array design in Section 3.3. As shown in Figure 8, the total efficiency could achieve over 90% in the frequency range of 23.15–26.43 GHz, and the maximum efficiency of 99% and realized gain of 11.8 dBi at broadside direction could be observed at 24.8 and 25.8 GHz, respectively. In addition, the beam scanning performance of the DRA array in two orthogonal planes is given in Figure 9. A −3 dB beam scanning angle of ±42°/±46° at the xz-/yz-plane could be observed when varying the excitation phases of the DRA elements. The simulated matching and radiation performance prove a promising beam scanning capacity of the designed DRA array in the 5G mmWave band.

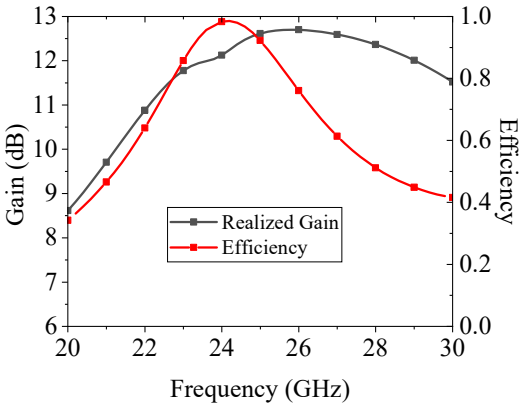

Figure 8. Simulated efficiency and realized gain for mmWave DRA array.

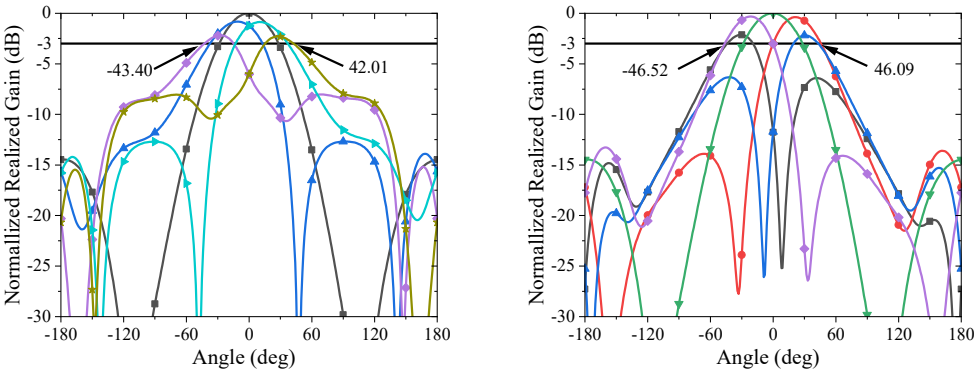

(**a**) (**b**)

Figure 9. Beam scanning performance of the DRA array in (**a**) xz- and (**b**) yz-plane.

3.1. Parametric Analysis for 3D Printing Process

In the 3D printing process for millimeter-wave applications, dimensional changes are expected during fabrication. The effects of these changes on various parameters of a standalone DRA are well documented. However, their impact when placed in an array has not been reported, particularly when taking into consideration the anticipated 3D-printing errors. It is important to note that we only consider uniform changes across all printed elements, assuming that the 3D printer will consistently produce deviations from the initial dimensions.

A parametric study was conducted in this section to investigate the impact of potential dimensional changes and errors when printing the DRA array on its electrical performance. The efficiency and realized gain instead of *S*-parameters were considered for this kind of multi-port array. The results for varied radius, height, permittivity (ε_r) and loss tangent (tan δ) of the DRA element are shown in Figures 10 and 11. The values used in the proposed mmWave DRA array are highlighted in bold. In FDM printing processes, the maximum expected fabrication error is approximately 0.2 mm, which corresponds to about 12.5% of the radius and 10.5% of the height for the mmWave DRA elements. Such errors can lead to an increase in resonant frequency of about 7.5% when increasing the radius and a 2.5% decrease when increasing the height. Additionally, as shown in Figure 10a,b, increasing the size of the DRAs results in lower realized gain. A reduction of 0.45 dB, from 12.7 dB to 12.45 dB, in maximum realized gain was observed when reducing the radius of the DRA element, whereas changes in the height had minimal effect, keeping the maximum realized gain nearly unchanged.

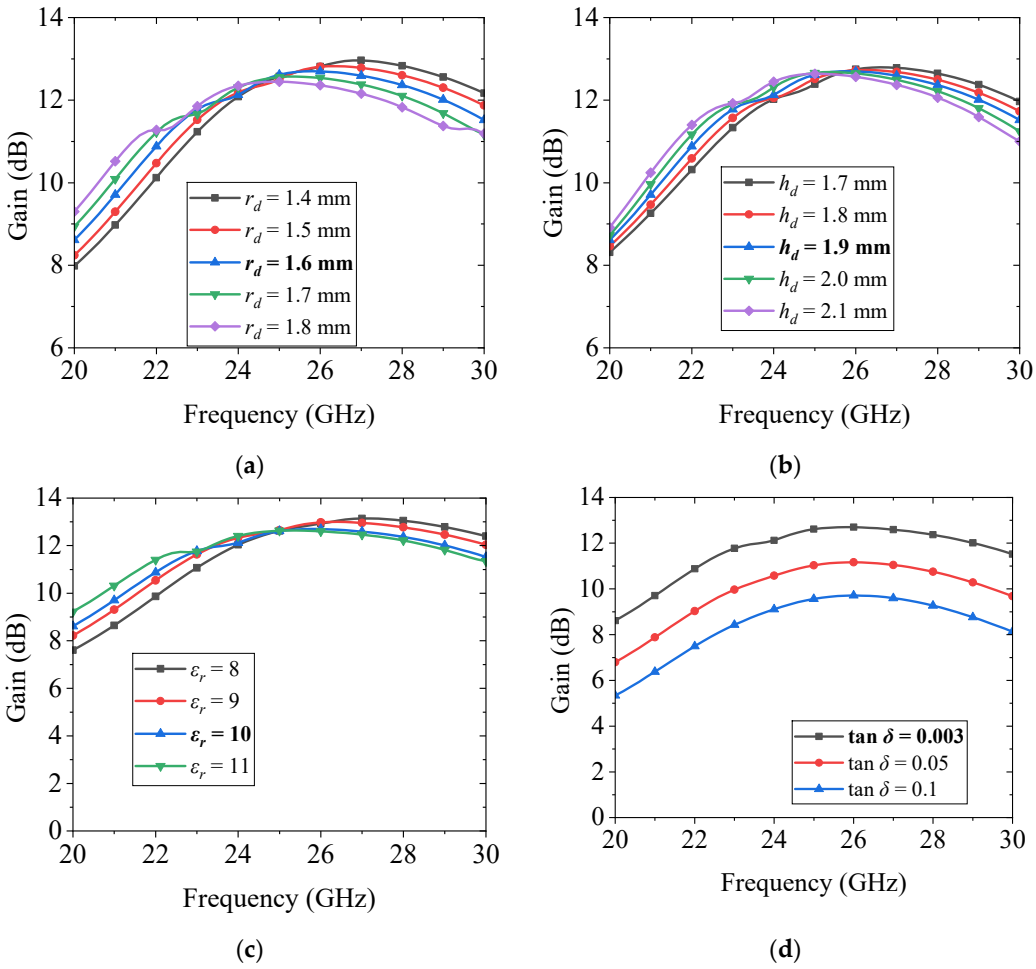

Figure 10. Gain at broadside direction with different (**a**) radius, (**b**) height, (**c**) ε_r, (**d**) tan δ of DRA element.

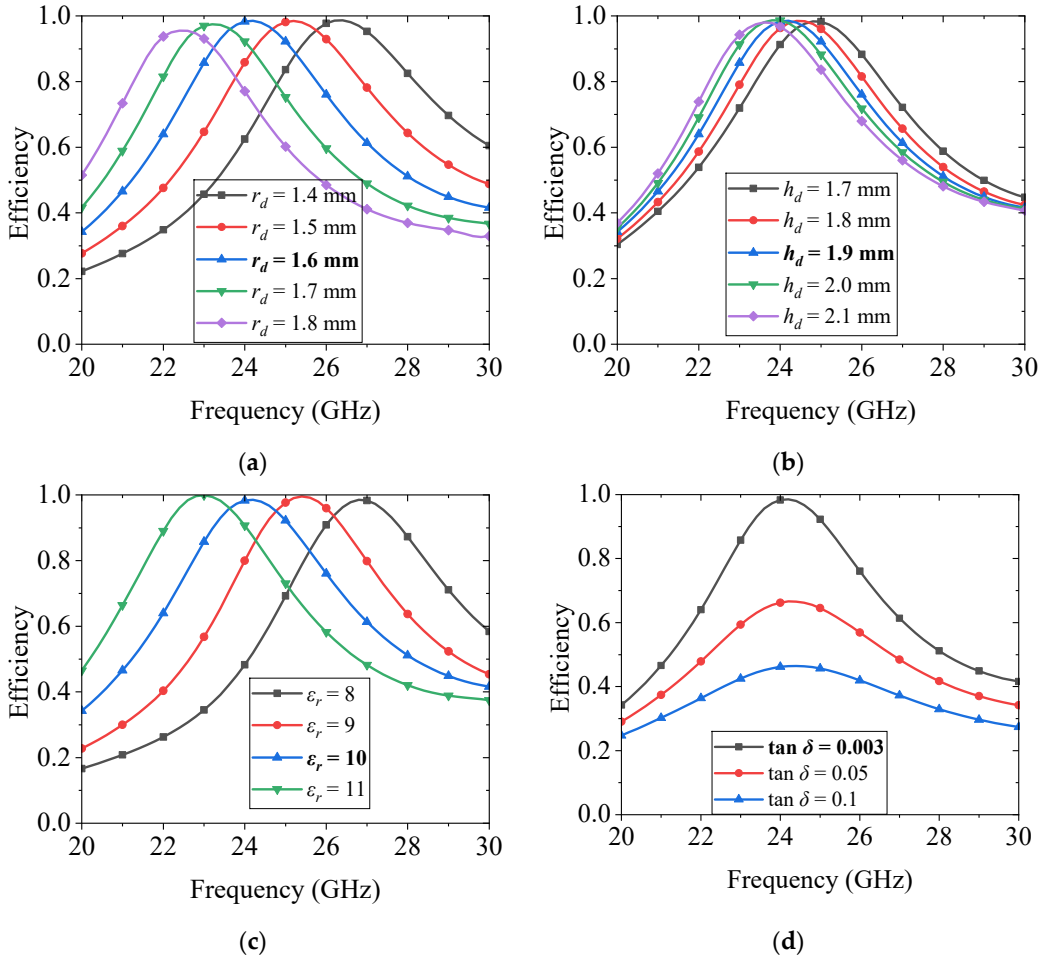

Figure 11. Efficiency with different (**a**) radius, (**b**) height, (**c**) ε_r, (**d**) tan δ of DRA element.

Unwanted air gaps introduced during the printing process can cause variations in the equivalent permittivity and loss tangent of the material. To assess the impact of these electrical properties, simulations were conducted. As depicted in Figures 10 and 11, the permittivity of the DRAs influences both the resonant frequency and the realized gain of the overall array, while the loss tangent primarily affects the realized gain. In the case of mmWave printed DRA antennas, the relative permittivity is likely to decrease due to gaps formed during fabrication, as observed in the previous section. A 10% decrease in relative permittivity leads to a 5% increase in resonant frequency. Additionally, this decrease in permittivity can increase the gain by about 0.3 dB. The loss tangent is also a crucial factor in determining antenna performance. Typically, PREPERM material maintains a consistent and relatively low loss tangent of 0.003. Air gaps introduced during fabrication can further reduce the loss tangent, resulting in slight improvements in gain and efficiency. However, any contamination of the filament or the use of more lossy materials can increase the loss tangent, significantly reducing both gain and efficiency. As illustrated in Figures 10d and 11d, an increase in the loss tangent to 0.1 causes the efficiency to drop from nearly 100% to 45%.

These results provide valuable insights into the effects and underlying causes of dimensional and material parameter variations on the array's radiation and impedance matching performance. Proper control of fabrication processes and material selection is critical for optimizing the performance of DRAs, especially at mmWave frequencies.

3.2. Fabrication and Measurements

For the purpose of verification, a 2 × 2 DRA array with an in-phase feeding network was manufactured, fabricated, and measured. The spacing between each two adjacent

DRA elements was optimized for a compromising efficiency and realized gain performance. The simulation model and fabricated photographs are shown in Figures 12 and 13, respectively. Considering the space for mounting the SMA connector, the overall dimension of the array was slightly enlarged and set to 26 mm × 26 mm × 2.1 mm, equivalent to 2.2 λ_0 × 2.2 λ_0 × 0.17 λ_0. However, it could be observed from the photos in Figure 13 that the overall dimension of the DRA array could be further reduced to make the array more compact. An equivalent model of the SMA connector was also considered in the simulation. The results indicate that the SMA connector has a limited effect on the array's performance. The DRA elements were manufactured using the Raise E2 3D printer and PREPERM® ABS1000 filament. A positioning resin mold, matching the exact dimensions of the substrate and featuring positioning holes for the DRA elements, was also fabricated to assist in the assembly of the DRA array.

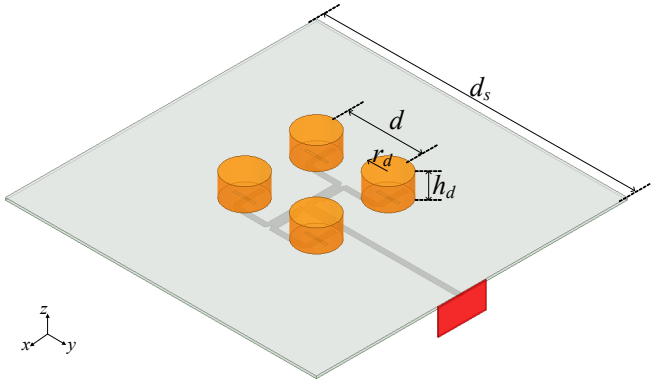

Figure 12. Configuration of the DRA array with an in-phase feeding network.

(**a**) (**b**)

Figure 13. Photographs of the FDM 3D-printed DRA array with an in-phase feeding network. (**a**) top view, (**b**) bottom view.

A 3D surface profile was also conducted for the mmWave DRA using the KEYENCE portable microscope (KEYENCE (UK) Ltd., Milton Keynes, UK). Some 3D surface profiles, zoom-in view profiles, and 2D profile cuts of the manufactured DRAs are shown in Figures 14–16. The shape generally agrees with the simulation model and relatively smooth surfaces were observed in the photos in Figure 15. Upon inspection of the profile, the diameter appears to be 0.2 mm to 0.3 mm, or about 8% larger than the simulated model when viewed from the top. This discrepancy may contribute to the observed frequency shift. Side bumps and dents resulting from printing layers were not measurable, as they were not observable in the downward-facing microscope view. Furthermore, several imperfections, one of which measures 152 µm, were observed, likely resulting from termination points in the printing process. A 3D side view and 2D cut surface profile of one of the mmWave DRA samples are shown in Figure 16. Protuberances with a maximum height (R_z) of 129.45 µm and an arithmetic average roughness (R_a) of 20.81 µm can be observed in the 3D side view and 2D cut surface profile shown in Figure 16. A total of nine layers, each 0.2 mm thick,

were necessary for constructing the microwave DRA model. However, the 3D design's required height of 1.9 mm is not a multiple of the typical FDM layer thickness (0.2 mm). This discrepancy arose from the measured height falling 0.1 mm short of the 3D simulated model. The imperfections created by the nine layers, along with other irregularities, became more conspicuous relative to the antenna's size at this frequency, compared to the microwave band.

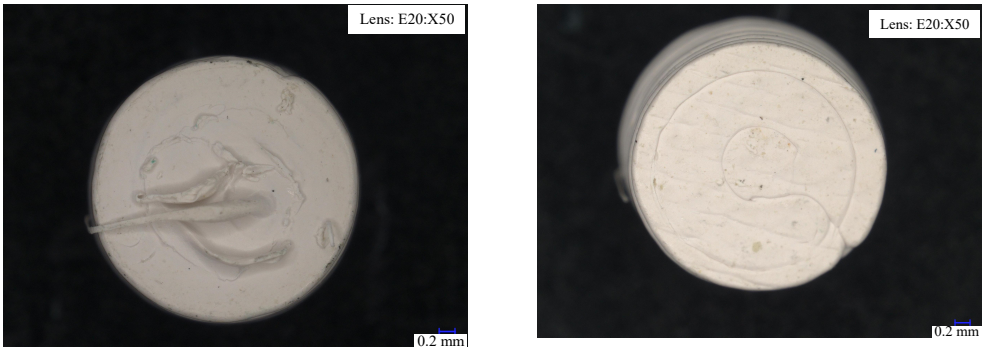

(**a**) (**b**)

Figure 14. Zoom-in view of the top and bottom surfaces of the FDM 3D-printed mmWave DRA. (**a**) top view, (**b**) bottom view.

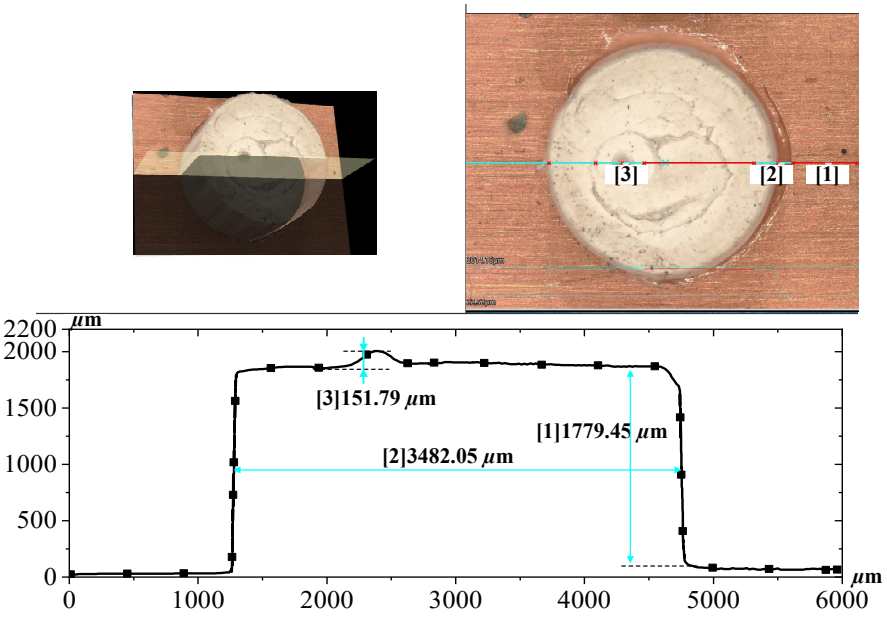

Figure 15. 2D cut surface profile of the FDM-printed mmWave DRA.

Taking this issue into account, a simulation was conducted with modified heights of the DRA elements. The *S*-parameters, far-field radiation patterns, and realized gain at the broadside direction of the FDM 3D-printed DRA array were then measured, and the results are given in Figures 17–19. As shown in Figure 17, the measured *S*-parameters indicate that the FDM 3D-printed DRA array could resonate within and cover the 5G mmWave frequency band. The simulated and measured Q factors are 21.43 and 57.27, respectively. Additionally, the modified simulation model with reduced height suggests that the possible cause of the frequency band shift is the change in element dimensions. The measured radiation patterns in both the xz- and yz-planes generally matched the simulated results, as shown in Figure 18, which indicates agreement between simulation and measurement. However, some discrepancies could still be observed. For example, there is an 8% shift to a lower band in the first resonant frequency, and the measured realized gain at the broadside

direction is about 2 dB lower than the simulated one. Differences in dimensional parameters could be part of the reason. Despite this, FDM 3D-printed DRAs at 5G mmWave frequencies fulfill design requirements, suggesting FDM as a viable option for DRA production.

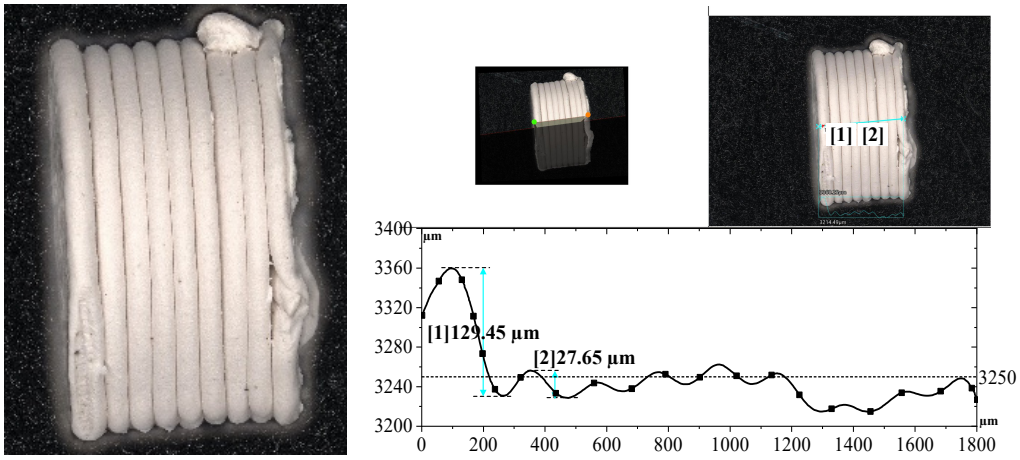

Figure 16. 3D side view and 2D cut surface profile of the FDM-printed mmWave DRA element.

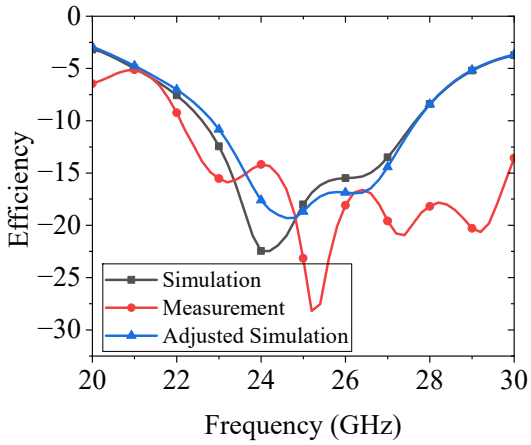

Figure 17. Simulated and measured matching performance of the FDM 3D-printed DRA array with in-phase feeding network.

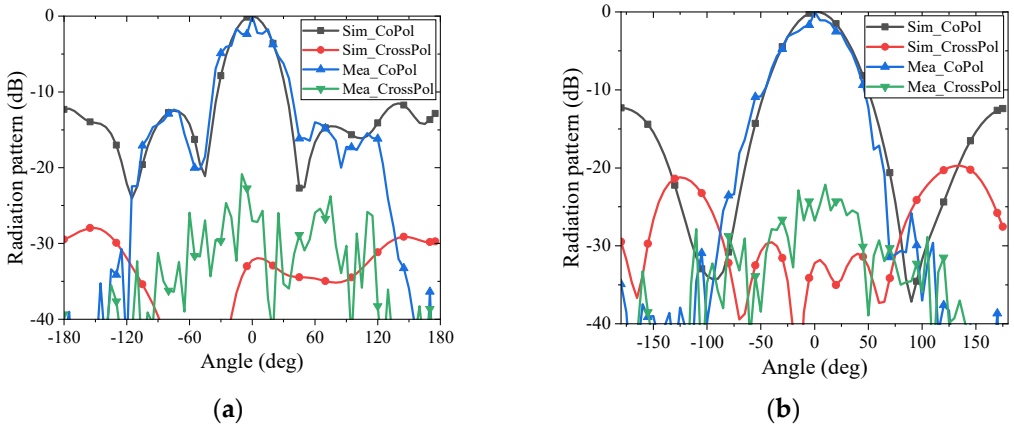

Figure 18. Simulated and measured radiation patterns of the FDM 3D-printed DRA array at 26.8 GHz. (**a**) xz- and (**b**) yz-plane.

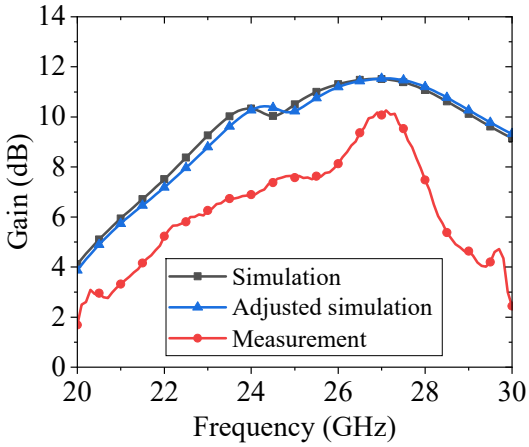

Figure 19. Simulated and measured realized gain at the broadside direction of the FDM 3D-printed DRA array.

3.3. Other Possible Solutions and Future Work

The cylindrical shape is very common in DRAs. However, other shapes can also be employed. In this section, we describe potential fabrication challenges associated with shapes that have sharper edges and corners, such as cuboids. The cuboid structure is presented as an array in RF simulations, and only the fabricated elements are discussed for potential issues in such designs.

To provide more insight into FDM 3D-printed DRAs at 5G mmWave frequencies, a 2 × 2 cuboid DRA array featuring beam scanning performance was also simulated, as shown in Figure 20. The substrate used is also Rogers RO4003 (ε_r = 3.55, tan δ = 0.0027) with a height of 0.2 mm. The DRA elements have a cuboid shape with dimensions of 2.5 mm × 2.5 mm × 2.0 mm. The total efficiency and gain at the broadside direction are shown in Figure 20b. A 90% efficiency frequency range of 25.38–29.66 GHz and a maximum realized gain of 11.5 dBi were observed. The beam scanning performance of the cuboid DRA array is shown in Figure 21. A −3 dB beam scanning angle of ±57°/±46° in the xz-/yz-planes can be observed when varying the excitation phases of the DRA elements. The simulated matching and radiation performance also prove the promising beam scanning capacity of the designed cuboid DRA array in the 5G mmWave band.

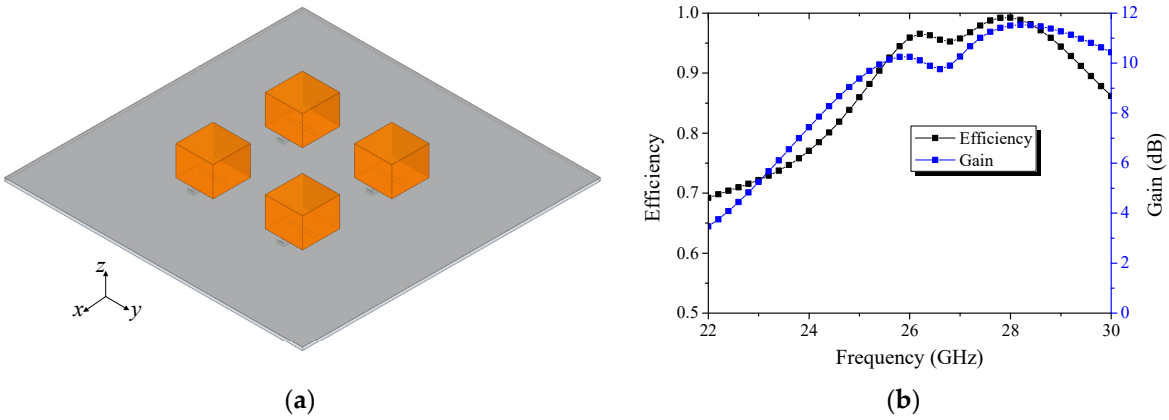

(**a**) (**b**)

Figure 20. (**a**) Configuration of the DRA array, and (**b**) simulated efficiency and realized gain.

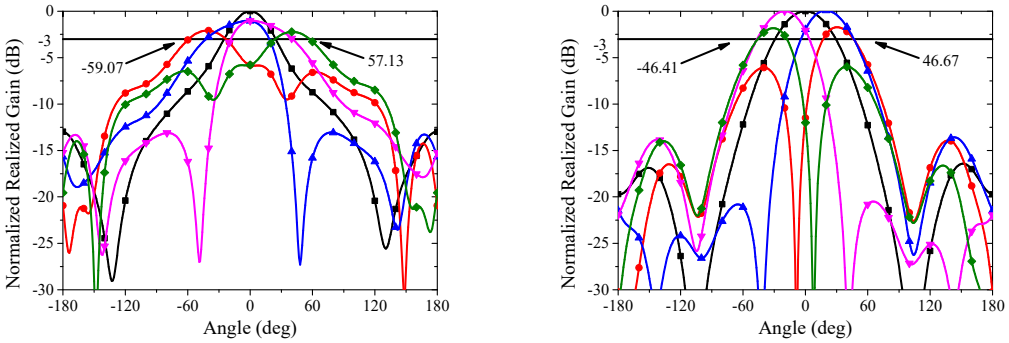

Figure 21. Beam scanning performance of the cuboid DRA array in the (**a**) xz-, and (**b**) yz-planes.

Some cuboid DRA elements were fabricated using an FDM 3D printer. Initially, the accuracy of the cuboid elements was not satisfactory due to the use of a 0.2 mm sacrificial PLA support between the antenna and the printing plate. Such sacrificial layers are typically used to facilitate printing and make part removal easier. This can be particularly useful for small parts, like mmWave DRA elements, when printing with special materials, as it helps prevent breakage during removal. The sacrificial layer is generally printed with low infill, around 20%, to ensure it can be easily removed. However, the use of this layer resulted in a slightly uneven surface at the base of the cuboid, which caused further deformations throughout the structure. This issue was resolved by printing the cuboid directly on the plate without support and adjusting the print settings accordingly. After this process, the resolution and dimensional accuracy of the DRA elements improved significantly, as shown in Figures 22 and 23. In the initial prints, visible gaps and hollows were observed on the top and side surfaces of the cuboid DRA, leading to considerable errors in the final structure. After refining the printing process, these air gaps were eliminated, and the layer stacks became smoother and more uniform. Additionally, the 10 layers of filament in the print accurately indicated the target height of 2.0 mm for the cuboid DRA.

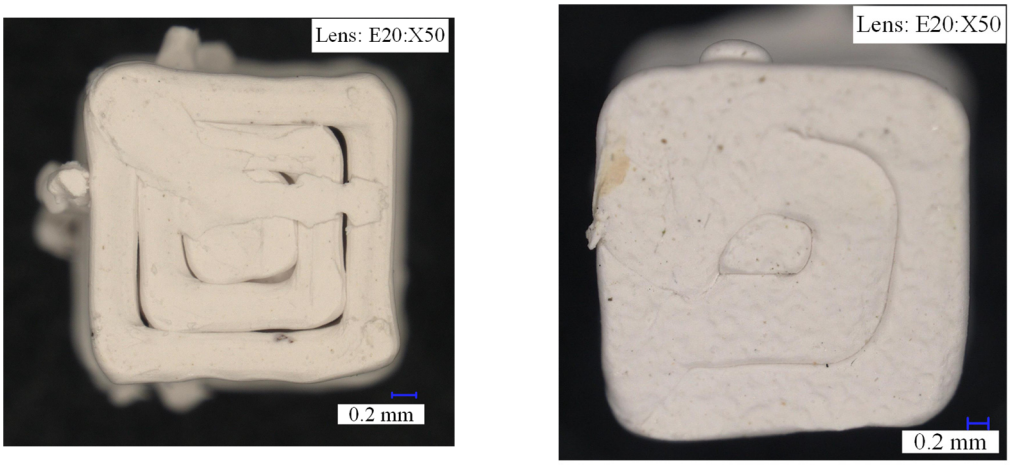

Figure 22. Top view of the FDM 3D-printed cuboid DRA element (**a**) before, and (**b**) after refining.

Despite the improvements, it was clear from the fabricated cuboid samples that achieving sharp edges and corners is challenging with the current FDM technique. The limitations of this method may result in slightly rounded corners or less-defined edges, which would affect the overall performance of the DRA. Further refinements in the fabrication process, such as exploring alternative 3D printing methods or higher-resolution settings, may be required to achieve the precision needed for sharper geometries in future designs.

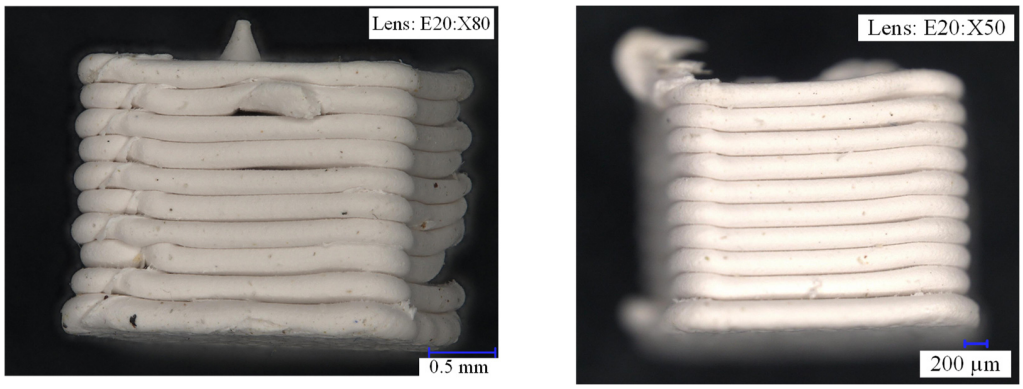

(**a**) (**b**)

Figure 23. Side view of the FDM 3D-printed cuboid DRA element (**a**) before, and (**b**) after refining.

4. Discussion and Conclusions

A comparison of different techniques for manufacturing DRAs was conducted, as shown in Table 1. Compared with conventional methods using dielectric ceramics and other additive manufacturing (AM) techniques, the applied FDM 3D printing technique emerges as a promising option. It offers a range of flexible material choices with variable electrical properties, making it highly adaptable to diverse applications. This approach presents several key advantages, including low cost, high resolution, rapid prototyping capabilities, and straightforward processing. These benefits enhance its viability for fabricating DRAs across different frequency bands, from microwave to mmWave. Additionally, as shown in Table 1, FDM does not provide the same high resolution as SLA. However, despite this, FDM's cost-effectiveness, material versatility, scalability, and ease of use make it an indispensable technology in the field of additive manufacturing. For applications where speed, practicality, and affordability are crucial, FDM is often the preferred choice, solidifying its continued importance in both research and industrial applications.

Table 1. Comparison with other techniques in producing DRAs.

Reference	**[3,4]**	**[33]**	**[34]**	**[35]**	**This Work**
Technique/Material	Dielectric ceramic	FDM/ PLA, polyamide, SLA/resin	FDM/3D printing filament	Micro-SLA/ photopolymer resin	FDM/ 3D printing filament
Working Frequency	Variable	3.5 GHz	1.575 GHz	3.5 GHz	13 GHz, 26 GHz
Permittivity	>20	6.41	15	2.7	10
Flexibleε_r? ε_rRange	No	No	Not given	No	Yes 2–12
Resolution	N.A.	0.2 mm	0.15 mm	25 µm	0.2 mm
Surface Roughness	N.A.	100 µm	N.A.	200 µm	<150 µm
Rapid Prototyping	No	Yes	Yes	Yes	Yes
Fabrication Steps	Multiple	Single	Single	Single	Single

Several DRA samples, including both cylindrical and cuboid geometries, were fabricated using FDM for operation at microwave and mmWave frequencies. The measured results and surface profiles confirm the feasibility of the FDM technique in manufacturing DRAs for modern 5G mmWave and beyond communication systems. Cylindrical DRAs, with their smoother surfaces and more consistent shape, exhibited fewer precision errors compared to cuboid DRAs, which showed challenges in achieving sharp edges and corners due to the inherent limitations of the FDM process. These challenges, while not critical at microwave frequencies, become more pronounced at higher mmWave frequencies, where small dimensional inaccuracies can significantly impact performance.

It is important to note that the precision of the printed DRAs, including dimensional tolerances and surface smoothness, becomes a critical factor when operating at higher mmWave frequencies. These slight deviations in geometry may restrict the application of FDM-printed DRAs in the upper mmWave bands. To address this, feedback from the fabrication process can be integrated into simulations, enabling a more consistent design and development process. By iterating between simulation and fabrication, it is possible to optimize the DRA design for specific applications, ensuring that the printed DRAs meet the necessary performance requirements despite the limitations of the 3D printing technique.

As the goal of this work was to assess the direct printing of the DRA for potential immediate use, no post-processing was applied. However, post-processing techniques, such as surface polishing, could reduce surface roughness and correct dimensional inaccuracies, potentially improving the final results. It is expected that future advances in FDM, as well as other 3D printing techniques, will allow for the fabrication of millimeter-wave DRA arrays at higher resolutions, which could also be integrated with 3D-printed circuits, including metallic conductive layers. Such technology for FDM printing of conductive and metallic layers already exists; however, it was not considered at this stage, as it would lead to significant deviations in performance at millimeter-wave frequencies. In the future, improvements in material science and multi-material 3D printing could allow for more seamless integration of dielectric, conductive, and flexible components within a single printing process. This would enable the development of fully 3D-printed, compact, and highly efficient antenna arrays, potentially reducing production costs and opening new applications in sectors such as 6G and beyond telecommunications, satellite systems, and IoT. Moreover, advances in printing at the nanoscale may further enhance the performance and miniaturization of millimeter-wave devices.

Author Contributions: Conceptualization, Z.C.; Investigation, S.L.; Supervision, B.S.I. and S.G. All authors have read and agreed to the published version of the manuscript.

Funding: This research was funded by EPSRC, grant number: EP/S005625/1, and Royal Society—International Exchanges 2019 Cost Share (NSFC), grant number: IEC\NSFC\191780.

Institutional Review Board Statement: Not applicable.

Informed Consent Statement: Not applicable.

Data Availability Statement: The data presented in this study are available on request from the corresponding author. The data are not publicly available due to no publicly accessible repository. But the authors would like to share the data included in the paper.

Acknowledgments: The authors would like to thank Antonio Mendoza, Keith Greenhow, Joseph Hill, and James Cridland (KEYENCE UK LTD) for their support.

Conflicts of Interest: The authors declare no conflict of interest.

References

1. Rahim, T.N.A.T.; Abdullah, A.M.; Md Akil, H. Recent Developments in Fused Deposition Modeling-Based 3D Printing of Polymers and Their Composites. *Polym. Rev.* **2019**, *59*, 589–624. [CrossRef]
2. Long, S.; Mcallister, M.; Shen, L. The resonant cylindrical dielectric cavity antenna. *IEEE Trans. Antennas Propag.* **1983**, *31*, 406–412. [CrossRef]
3. Shehbaz, M.; Du, C.; Zhou, D.; Xia, S.; Xu, Z. Recent progress in dielectric resonator antenna: Materials, designs, fabrications, and their performance. *Appl. Phys. Rev.* **2023**, *10*, 021303. [CrossRef]
4. Liang, J.; Lu, W.-Z.; Wu, J.-M.; Guan, J.-G. Microwave dielectric properties of Li2TiO3 ceramics sintered at low temperatures. *Mater. Sci. Eng. B* **2011**, *176*, 99–102. [CrossRef]
5. Haghzadeh, M.; Armiento, C.; Akyurtlu, A. All-Printed Flexible Microwave Varactors and Phase Shifters Based on a Tunable BST/Polymer. *IEEE Trans. Microw. Theory Tech.* **2017**, *65*, 2030–2042. [CrossRef]
6. Lee, S.-E.; Choi, S.P.; Oh, K.-S.; Kim, J.; Lee, S.M.; Cho, K.R. Flexible Magnetic Polymer Composite Substrate with Ba1.5Sr1.5Z Hexaferrite Particles of VHF/Low UHF Patch Antennas for UAVs and Medical Implant Devices. *Materials* **2020**, *13*, 1021. [CrossRef]
7. Kremer, H.I.; Leung, K.W.; Wong, W.C.; Lo, K.K.-W.; Lee, M.W.K. Design of Dielectric Resonator Antenna Using Dielectric Paste. *Sensors* **2021**, *21*, 4058. [CrossRef]

8. Jang, D.; Lee, J.-Y.; Choo, H. Design of a Stacked Dual-Patch Antenna with 3D Printed Thick Quasi-Air Substrates and a Cavity Wall for Wideband Applications. *Appl. Sci.* **2024**, *14*, 1571. [CrossRef]
9. Benkhadda, O.; Ahmad, S.; Saih, M.; Chaji, K.; Reha, A.; Ghaffar, A.; Khan, S.; Alibakhshikenari, M.; Limiti, E. Compact Broadband Antenna with Vicsek Fractal Slots for WLAN and WiMAX Applications. *Appl. Sci.* **2022**, *12*, 1142. [CrossRef]
10. Lee, S.; Yang, Y.; Lee, K.-Y.; Jung, K.-Y.; Hwang, K. Robust Design of 3D-Printed 6–18 GHz Double-Ridged TEM Horn Antenna. *Appl. Sci.* **2018**, *8*, 1582. [CrossRef]
11. Popela, M.; Olivová, J.; Plíva, Z.; Petržílka, L.; Krchová, M.; Joska, Z.; Janů, P. A Novel Approach to the Production of Printed Patch Antennas. *Appl. Sci.* **2024**, *14*, 1556. [CrossRef]
12. Melchiorre, L.; Marasco, I.; Niro, G.; Basile, V.; Marrocco, V.; D'Orazio, A.; Grande, M. Bio-Inspired Dielectric Resonator Antenna for Wideband Sub-6 GHz Range. *Appl. Sci.* **2020**, *10*, 8826. [CrossRef]
13. Shastri, A.; Sanz-Izquierdo, B.; Elibiary, A.; Parker, E.A. Manufacturing, Developments, and Constraints in Full 3-D Printing of Frequency-Selective Surface Using Low-Cost Open-Source Printer. *IEEE Trans. Compon. Packag. Manuf. Technol.* **2021**, *11*, 2193–2200. [CrossRef]
14. Adamec, B.; Machaj, J.; Brida, P.A. Novel Wideband Splitter for a Four-Element Antenna Array. *Appl. Sci.* **2024**, *14*, 1593. [CrossRef]
15. Zhu, J.; Yang, Y.; Li, M.; Mcgloin, D.; Liao, S.; Nulman, J.; Yamada, M.; Iacopi, F. Additively Manufactured Millimeter-Wave Dual-Band Single-Polarization Shared Aperture Fresnel Zone Plate Metalens Antenna. *IEEE Trans. Antennas Propag.* **2021**, *69*, 6261–6272. [CrossRef]
16. Zhu, J.; Yang, Y.; Hu, N.; Liao, S.; Nulman, J. Additively Manufactured Multi-Material Ultrathin Metasurfaces for Broadband Circular Polarization Decoupled Beams and Orbital Angular Momentum Generation. *ACS Appl. Mater. Interfaces* **2021**, *13*, 59460–59470. [CrossRef]
17. Attaran, M. The rise of 3-D printing: The advantages of additive manufacturing over traditional manufacturing. *Bus. Horiz.* **2017**, *60*, 677–688. [CrossRef]
18. Ngo, T.D.; Kashani, A.; Imbalzano, G.; Nguyen, K.T.; Hui, D. Additive manufacturing (3D printing): A review of materials, methods, applications and challenges. *Compos. Part B Eng.* **2018**, *143*, 172–196. [CrossRef]
19. Gokuldoss, P.K.; Kolla, S.; Eckert, J. Additive Manufacturing Processes: Selective Laser Melting, Electron Beam Melting and Binder Jetting-Selection Guidelines. *Materials* **2017**, *10*, 672. [CrossRef]
20. Djurović, S.; Lazarević, D.; Ćirković, B.; Mišić, M.; Ivković, M.; Stojčetović, B.; Petković, M.; Ašonja, A. Modeling and Prediction of Surface Roughness in Hybrid Manufacturing–Milling after FDM Using Artificial Neural Networks. *Appl. Sci.* **2024**, *14*, 5980. [CrossRef]
21. Meana, V.; Zapico, P.; Cuesta, E.; Giganto, S.; Meana, L.; Martínez-Pellitero, S. Additive Manufacturing of Ceramic Reference Spheres by Stereolithography (SLA). *Appl. Sci.* **2024**, *14*, 7530. [CrossRef]
22. Pozhanka, M.; Zagrai, A.; Baez Avila, F.; Drach, B. Application of Ultrasonic Testing for Assessing the Elastic Properties of PLA Manufactured by Fused Deposition Modeling. *Appl. Sci.* **2024**, *14*, 7639. [CrossRef]
23. Kumar, S.; Kruth, J.-P. Composites by rapid prototyping technology. *Mater. Des.* **2010**, *31*, 850–856. [CrossRef]
24. Mur-Gorgas, A.; Martínez-Pellitero, S.; Joglar, T.; Escapa, A.; Mateos, R. 3D-Printed Conductive Polymers as Alternative for Bioelectrochemical Systems Electrodes: Abiotic Study and Biotic Start-Up. *Appl. Sci.* **2024**, *14*, 7199. [CrossRef]
25. Öngül, F.F.; Kandemir, İ.; Pala Öngül, E. Experimental Comparison of Fastener Implementation Approaches in Fused Deposition Modeling. *Appl. Sci.* **2024**, *14*, 5172. [CrossRef]
26. Vido, M.; De Oliveira Neto, G.C.; Lourenço, S.R.; Amorim, M.; Rodrigues, M.J.F. Computer-Aided Design and Additive Manufacturing for Automotive Prototypes: A Review. *Appl. Sci.* **2024**, *14*, 7155. [CrossRef]
27. Massaccesi, A.; Bertana, V.; Beccaria, M.; Marasso, S.L.; Cocuzza, M.; Dassano, G.; Pirinoli, P. Three-Dimensional-Printed Wideband Perforated Dielectric-Only Reflectarray in Ka-Band. *IEEE Trans. Antennas Propag.* **2023**, *71*, 7848–7859. [CrossRef]
28. Melendro-Jiménez, J.; Sanchez-Olivares, P.; Tamayo-Domínguez, A.; Luis Masa-Campos, J.; Fernández-González, J.-M. A Novel Logarithmic-Spiral-Shaped 3-D-Printed Dielectric Polarizer for Dual-Circularly Polarized Conical-Beam Radiation Patterns in the Ka-Band. *IEEE Trans. Antennas Propag.* **2024**, *72*, 6219–6228. [CrossRef]
29. Melendro-Jimenez, J.; Sanchez-Olivares, P.; Tamayo-Dominguez, A.; Sun, X.; Fernandez-Gonzalez, J.M. 3D Printed Directive Beam-Steering Antenna Based on Gradient Index Flat Lens With an Integrated Polarizer for Dual Circular Polarization at W-Band. *IEEE Trans. Antennas Propag.* **2023**, *71*, 1059–1064. [CrossRef]
30. Wang, Y.; Han, M.; Dou, W.; Li, T. 3-D-Printed All-Metal Conformal Circularly Polarized Reflectarray Antenna at X-Band. *IEEE Trans. Antennas Propag.* **2024**, *72*, 4989–4998. [CrossRef]
31. Li, S.; Izquierdo, B.S.; Gao, S.; Chen, Z. 3D-Printed Dielectric Resonator Antenna Array for Millimeter Wave Applications. In Proceedings of the 2023 International Conference on Microwave and Millimeter Wave Technology (ICMMT), Qingdao, China, 14–17 May 2023.
32. Li, S.; Njogu, P.; Izquierdo, B.S.; Gao, S.; Chen, Z. 3D Printing Antennas for 5G and Millimeter Wave 6G Applications. In Proceedings of the 2022 IEEE 33rd Annual International Symposium on Personal, Indoor and Mobile Radio Communications (PIMRC), Virtual, 12–15 September 2022.

33. Marrocco, V.; Basile, V.; Fassi, I.; Grande, M.; Laneve, D.; Prudenzano, F.; D'Orazio, A. Dielectric Resonant Antennas via Additive Manufacturing for 5G Communications. In Proceedings of the 2019 PhotonIcs & Electromagnetics Research Symposium-Spring (PIERS-Spring), Rome, Italy, 1 June 2019.
34. Hehenberger, S.P.; Caizzone, S.; Yarovoy, A.G. Additive Manufacturing of Linear Continuous Permittivity Profiles and Their Application to Cylindrical Dielectric Resonator Antennas. *IEEE Open J. Antennas Propag.* **2023**, *4*, 373–382. [CrossRef]
35. Basile, V.; Grande, M.; Marrocco, V.; Laneve, D.; Petrignani, S.; Prudenzano, F.; Fassi, I. Design and Manufacturing of Super-Shaped Dielectric Resonator Antennas for 5G Applications Using Stereolithography. *IEEE Access* **2020**, *8*, 82929–82937. [CrossRef]
36. Ferrando-Rocher, M.; Herranz-Herruzo, J.I.; Valero-Nogueira, A.; Bernardo-Clemente, B. Selective Laser Sintering Manufacturing as a Low Cost Alternative for Flat-Panel Antennas in Millimeter-Wave Bands. *IEEE Access* **2021**, *9*, 45721–45729. [CrossRef]
37. Huang, G.-L.; Zhou, S.-G.; Chio, T.-H.; Yeo, T.-S. Fabrication of a High-Efficiency Waveguide Antenna Array via Direct Metal Laser Sintering. *IEEE Antennas Wirel. Propag. Lett.* **2016**, *15*, 622–625. [CrossRef]
38. Huang, G.-L.; Zhou, S.-G.; Yuan, T. Development of a Wideband and High-Efficiency Waveguide-Based Compact Antenna Radiator With Binder-Jetting Technique. *IEEE Trans. Compon. Packag. Manuf. Technol.* **2017**, *7*, 1–7. [CrossRef]
39. Oh, Y.; Bharambe, V.; Mummareddy, B.; Martin, J.; McKnight, J.; Abraham, M.A.; Walker, J.M.; Rogers, K.; Conner, B.; Cortes, P. Microwave dielectric properties of zirconia fabricated using NanoParticle Jetting™. *Addit. Manuf.* **2019**, *27*, 586–594. [CrossRef]
40. Volakis, J.L.; Johnson, R.C.; Jasik, H. *Antenna Engineering Handbook*; McGraw-Hill: New York, NY, USA, 2007.
41. *ISO 4287*; Geometrical Product Specifications (GPS)—Surface Texture: Profile Method—Terms, Definitions and Surface Texture Parameters, 2nd ed. International Organization for Standardization: Geneva, Switzerland, 1997.